Journal of Power Sources 206 (2012) 119–128

Contents lists available at SciVerse ScienceDirect

Journal of Power Sources

journal homepage: www.elsevier.com/locate/jpowsour

Droplet dynamics in a polymer electrolyte fuel cell gas flow channel: Forces, deformation, and detachment. I: Theoretical and numerical analyses

Sung Chan Cho [a], Yun Wang [a,*], Ken S. Chen [b]

[a] Renewable Energy Resources Lab (RERL) and National Fuel Cell Research Center, Department of Mechanical and Aerospace Engineering, The University of California, Irvine, Irvine, CA 92697-3975, USA
[b] Sandia National Laboratories, 7011 East Avenue, MS9154 Livermore, CA 94580, USA

ARTICLE INFO

Article history:
Received 12 November 2011
Accepted 4 January 2012
Available online 28 January 2012

Keywords:
Droplet dynamics
Detachment
Deformation
Micro channel
Theoretical analysis
Numerical

ABSTRACT

Water management is critical to achieving/maintaining high performance of polymer electrolyte fuel cells (PEFCs); and elucidating the dynamic behavior of liquid water droplets in a PEFC channel is essential to water management. In this work, the dynamics of liquid water droplets in a single PEFC gas flow channel is investigated through theoretical and numerical analyses. Forces on water droplet, droplet deformation and detachment are examined. The pressure and viscous drags are computed and compared at different flow regimes (which exhibit different droplet-dynamic scenarios) such as that in the entrance and fully developed flow regions. The expression for describing droplet shape change is derived, and it is found that the droplet can deform significantly at high gas-flow rates and when the droplet is relatively large (relative to the channel dimension). The detachment velocity is analyzed by comparing the wall adhesion and drag forces, and an expression relating the Weber number to the Reynolds number using the detachment velocity is developed. Follow-on work is also briefly discussed.

1. Introduction

Water management is one of the key issues in polymer electrolyte fuel cells (PEFCs): appropriate humidification is critical to achieving high ionic conductivity of membrane whereas excessive water causes flooding and consequently reduces cell performance. In the gas flow channel, droplets can form at the hydrophobic GDL (gas diffusion layer) surfaces and hinder the transport of oxygen and hydrogen towards the respective catalyst layers where the electrochemical reactions occur [1–4].

Liquid water can be produced in the cathode catalyst layer by the oxygen-reduction electrochemical reaction ($\frac{1}{2}O_2 + 2H^+ + 2e^- \leftrightarrow H_2O$) or in the components where condensation occurs [5–7] when the local temperature reaches the dew point. Liquid water can transport through the porous media, which is driven by the capillary force or through the membrane by the hydraulic permeation. Liquid water will eventually reach the interfaces between the gas flow channels (GFCs) and gas diffusion layers (GDLs), where it either forms droplets at the GDL surface or attaches to the hydrophilic channel wall [8]. Liquid water in the GFC can block local channels and thus reduce fuel cell performance. Wang et al. [9] indicated that the voltage fluctuation occurred when the flow stoichiometry ratio is reduced to around 2 at which the air flow rate is insufficient to remove liquid water. Due to the GDL surface roughness and contact angle hysteresis, droplets can be held by surface-tension forces on the GDL surface, and grow their bulk volume until they are removed by the gas-phase reactant flow [10–12]. Several factors such as the gas-phase velocity, droplet diameter, contact angle, contact-angle hysteresis and gas flow properties can affect droplet detachment. Droplets can be deformed by the forces imposed by gas flows, which can modify its projected area and hence the drag force [13–16]. The presence of droplets increases the gas flow pressure drop. Adroher and Wang [17] reported that the two-phase pressure amplifier can be as high as 10 at low gas flow velocity ($<0.5\,m\,s^{-1}$). They also presented model analysis and compared their predictions with that reported by others.

Several numerical and analytical approaches have been proposed to elucidate droplet removal on the GDL surface. Chen et al. [13,14] provided simplified models for prediction of droplet detachment velocity, respectively, in the low-Reynolds number (Re) regime (in which inertia is negligible) and in the inertia-dominating regime ($Re \sim 1000$). The models by Chen et al. account for the effects of static contact angle, contact angle hysteresis and gas-phase velocity on detachment velocity. Avoidance of channel lodging was also studied for both cylindrical and spherical droplets. Kumbur et al. [15] presented a similar analytical method for droplet instability with focus on the contact-angle hysteresis. The effects of PTFE contents in MPL (micro porous layer) and Reynolds number on the contact-angle hysteresis were investigated. Theodorakakos

* Corresponding author. Tel.: +1 949 824 6004; fax: +1 949 824 8585.
E-mail address: yunw@uci.edu (Y. Wang).

0378-7753/$ – see front matter © 2012 Elsevier B.V. All rights reserved.
doi:10.1016/j.jpowsour.2012.01.057

Nomenclature

A	area (m^2)
a	coefficient for correlation
b	coefficient for correlation
D, d	droplet diameter (m, mm)
D_H	hydraulic diameter (m)
Eö	Eötvos number
F	force (N)
g	gravitational acceleration ($m\,s^{-2}$)
H	channel height (m)
h_d	droplet height (m)
$\hat{i}$	direction vector
I	unit tensor
L	channel length (m)
L_E	entrance length (m)
$\hat{n}$	normal vector
p	pressure (pa)
R	local curvature (m)
r	droplet radius (m)
RH	relative humidity
U, u	velocity ($m\,s^{-1}$)
W	channel width (m)
We_r	Weber number

Greek letters

α	Volume fraction
γ	Surface tension ($N\,m^{-1}$)
ζ	area ratio
θ	contact angle (rad,°)
μ	viscosity ($kg\,(m\,s)^{-1}$)
ρ	density ($kg\,m^{-3}$)

Subscript

a	advancing
d	droplet
c	critical
H	hysteresis
in	inlet
press	pressure
r	receding
s	static
visco	viscosity

et al. [16] studied water-droplet deformation under cross-flowing air both experimentally and numerically. In their work, contact angles measured experimentally were compared to that predicted by the VOF (Volume of Fluid) method. He et al. [18] suggested a simple analytical model to predict the size of single droplet for detachment under certain air flow velocity. Between advancing and receding contact angles, continuous contact-angle change along with circular contact line was considered. The effect of GDL hydrophobicity and surface tension on detachment was studied by He et al. Schillberg and Kandlikar [19] provided a comprehensive review on analytical models for droplet detachment mechanism and suggested considering more accurate geometry (droplet projected area, droplet surface area) for force estimation to enhance the analytic models.

Droplet formation occurs in the two-phase region, where the gas flow reaches the saturated state. Wang [8] gave the prediction of the onset of two-phase flow when dry air is used. Droplets tend to form in preferential sites after the flowing gas mixture reaching the saturated state and they are not uniformly distributed along the channel [20,21]. Ous and Arcoumamis [21] studied the effect of air velocity, relative humidity and external load of fuel cells in the presence and removal of water droplet through visualization. Droplets are formed non-uniformly along the channel and air velocity is inversely proportional to the detachment droplet dimension. Shirani and Masoomi [22] studied the main factors of 2-D droplet deformation by using the VOF-PCIL method. It is found that droplet deformation in the air flow direction is highly related to the capillary number. Zhu et al. [23,24] used the 2-D and 3-D VOF methods to investigate the impact of pore and channel geometry on droplet dynamics. Fang et al. [25] emphasized the importance of contact-angle hysteresis on detachment velocity, showing that the VOF without taking into account of contact-angle hysteresis can cause low detachment velocity.

Despite previous efforts, a comprehensive study on droplet dynamics that delineates the forces over a droplet at different regions of channel flows, and theoretical analysis on droplet deformation and detachment is highly needed. In this work, we examine the forces over a droplet at various conditions and different locations. Analysis is performed to predict water droplet deformation, and numerical models of droplet detachment are also introduced. The influence of droplet diameter, gas-phase velocity, and location of liquid droplet are presented for both air and hydrogen flow fields. We will compare the analytical solutions of the droplet deformation and removal with experimental data and the VOF simulation prediction in a sequel paper.

2. Droplet dynamics

In this section, three major topics of droplet dynamics are described and discussed, which are important to elucidating droplet behaviors in PEFC gas flow channels.

2.1. Forces on a liquid water droplet

A water droplet on the GDL surface in the gas flow channel experiences drag forces exerted by the surrounding gas flow. Since channel flow is viscous, the sharp change of the gas velocity near the droplet surface causes a drag force over the droplet. Drag force can also arise from the gas pressure: the upstream has a higher pressure, leading to the pressure drag. In the gas-flow channel of a PEFC, the surface tension is usually a dominant factor that controls the liquid-droplet shape. Adamson and Gast [27] examined the free droplet shape considering surface tension and gravitational force in static air. The effect of the gravitational force is usually small for droplets with diameters on the order of a few hundred microns in a millimeter-sized channel, which can be explained using the Eötvos number defined as:

$$\text{Eö} = \frac{\Delta\rho g d^2}{\gamma} \tag{1}$$

The cases considered in the present work show a relatively low Eötvos number (Eö: 0.0015–0.15) with which the gravitational effect is negligible [30]. Consequently, the droplet shape in slow air flow can be assumed, to a good approximation, to be spherical and has a constant curvature at any local point. Fig. 1 shows the force balance on a spherical liquid droplet. At the onset of detachment (that is, immediately before the droplet is detached), all forces on a droplet, including the wall adhesion, are balanced to keep the droplet stationary. The drag, created by air flows near the droplet, is the sum of the pressure and viscous forces. The pressure force can be calculated by:

$$F_{\text{press}} = \hat{i} \cdot \int_A \hat{n} \cdot p \; dA \tag{2}$$

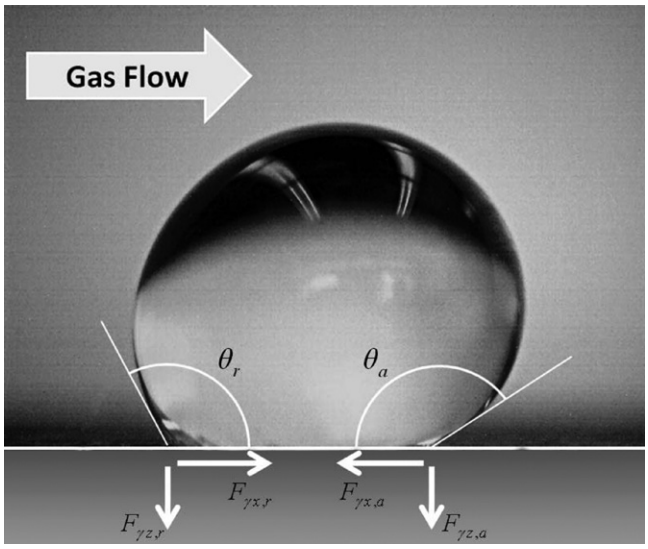

Fig. 1. Force balance on a liquid water droplet on a hydrophobic wall.

where $\hat{i}$ is the direction vector of gas flow, $\hat{n}$ the normal vector of the infinitesimal surface, p local pressure and A the area of droplet surface. By employing CFD (computational fluid dynamics) with a fine mesh, the pressure distribution on the droplet surface can be integrated over the droplet surface in the flow direction to compute the drag force caused by pressure. Another force, the viscous friction at the gas–liquid interface, can be evaluated by:

$$F_{\text{visco}} = \hat{i} \cdot \int_A \mu_{\text{gas}} \nabla u \; dA \tag{3}$$

The local velocity gradient is calculated based on the CFD results of the velocity field. The total drag is then the summation of pressure force and viscous force:

$$F_{\text{drag}} = F_{\text{press}} + F_{\text{visco}} \tag{4}$$

Wall adhesion (or force arising from surface tension) can be divided into the normal (z-direction) and tangential (x-direction) components. The maximum tangential force is determined by the static contact angle (θ_s), contact-angle hysteresis (θ_H) and surface tension (γ) [13]:

$$F_{\gamma x} = F_{\gamma x,\text{r}} + F_{\gamma x,\text{a}} = 2\gamma\pi d \cdot \sin^2 \; \theta_s \cdot \sin\frac{\theta_H}{2} \tag{5}$$

For the hydrophobic GDL surface, the effects of advancing and receding angles are opposite to each other and thus partly canceled out. When there is surrounding gas flow, the advancing angle is greater than receding angle, making the combined wall adhesion opposite to the gas flow direction. The normal wall adhesion can be estimated by integrating the adhesion force over the contact line of the droplet and wall:

$$F_{\gamma z} = 2\gamma \cdot \left(\pi\frac{d}{2}\sin\;\theta_s\right) \cdot \int_0^{\pi} \sin\left(\theta_r + \frac{\theta_a - \theta_r}{\pi}\phi\right) d\phi \tag{6}$$

ϕ is the angle of the projected circle on the GDL surface. In the present work, a simple relation is adopted between the static contact angle and contact-angle hysteresis:

$$\theta_r = \theta_s - \frac{\theta_a - \theta_r}{2} \tag{7}$$

A local contact angle ξ can be defined along the contact line on the GDL surface as [15]:

$$\xi = \theta_r + \frac{\theta_a - \theta_r}{\pi}\phi \tag{8}$$

Eq. (6) can be re-organized as:

$$F_{\gamma z} = 2\gamma \cdot \left(\pi\frac{d}{2}\sin\theta_s\right) \cdot \left(\int_{\theta_r}^{\theta_a} \sin\xi\frac{\pi}{\theta_H}d\xi\right) \cdot \frac{1}{\pi}$$

$$= 2\gamma\frac{\pi}{\theta_H}d \cdot \sin\;\theta_s \cdot \sin\frac{\theta_s}{2} \cdot \sin\frac{\theta_H}{2} \tag{9}$$

This force component is the maximum that can balance the lift force over the droplet due to the surrounding flow. When the lift force overcomes this barrier, the droplet will be detached from the surface. The criteria for water droplet detachment can be defined by considering two directions:

$$F_{\text{drag}} > F_{\gamma x} \tag{10}$$

$$F_{\text{Lift}} > F_{\gamma z} \tag{11}$$

Satisfaction of either of the two criteria will lead to droplet detachment. In reality, the second criterion is more difficult to satisfy than the first one. Thus, the first criterion is frequently used for droplet detachment analysis and the critical condition, i.e. $F_{\text{drag}} = F_{\gamma x}$, can be expressed by:

$$\hat{i} \cdot \int_A (\hat{n} \cdot p + \mu_{\text{gas}}\nabla u)dA = 2\gamma\pi d \cdot \sin^2\theta_s \cdot \sin\frac{\theta_H}{2} \tag{12}$$

2.2. Droplet deformation due to pressure variation

Droplets can be deformed by the forces exerted by the surrounding air flow, causing the droplet to deviate away from the spherical shape [22–25]. There are two major forces by air flow: one is the viscous force, the other is pressure variation. The former is due to the viscosity of air (hydrated with liquid water), which causes the sharp change of velocity near the droplet surface, and is usually along the tangential direction at the surface. This force highly depends on the local flow field and can vary greatly when air flow condition changes. At a high air flow rate, backward air flows can develop near the liquid surface. The other force results from the droplet obstruction which causes the pressure variation over the droplet surface. The pressure difference at two typical sites can be estimated: one is at the droplet front where the flow is stagnated; the other is at the side where the air flow cross section reaches a local minimum. The air pressure will also change in corresponding to the velocity change. The pressure change will alter the local curvature of the droplet. Fig. 2 shows schematic of a liquid droplet in a gas flow channel. The local curvature of the droplet can be calculated by the Young-Laplace Equation:

$$p_{\text{liq}} - p_{\text{gas}} = \frac{2\gamma}{R} \tag{13}$$

Assuming a constant liquid pressure throughout the droplet at steady state, Eq. (13) can be differentiated to evaluate the impact of the gas pressure variation dp_{gas} on the local curvature:

$$\frac{dR}{R} = \frac{R}{2\gamma}dp_{\text{gas}} \tag{14}$$

where R is the local curvature of the gas–liquid interface. Evaluation of dp_{gas} can follow that in the orifice plates or Venturi tubes [26]: based on the Bernoulli's principle, the gas-phase pressure drop is proportional to the square of air velocity and the local averaged gas velocity can be computed using the mass conservation. To better elucidate the issue, we also consider a 2-D case, which assumes the channel only has finite dimensions in the along-channel and height directions, and a 2-D droplet has a shape similar to a cylinder. The area ratio (ζ) between upstream and on the droplet for 2-D and 3-D

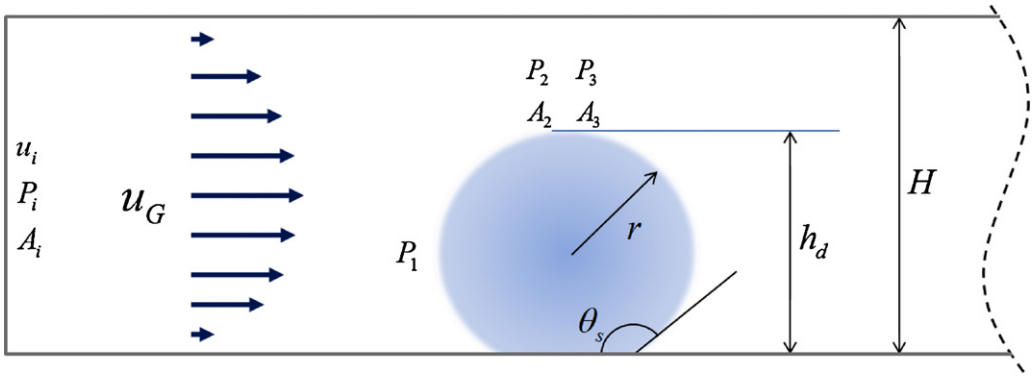

Fig. 2. Schematic of a liquid water droplet in a 2-D and 3-D micro gas channel.

can be evaluated by:

$$\text{2-D}: \quad \zeta_{2D} = \frac{A_i}{A_2} = \frac{W \times H}{W \times [H - R_0(1 - \cos\theta_s)]} = \frac{H}{H - R_0(1 - \cos\theta_s)} \tag{15}$$

$$\text{3-D}: \quad \zeta_{3D} = \frac{A_i}{A_3} = \frac{W \times H}{W \times H - R_0^2(\theta_s - \cos\theta_s \sin\theta_s)} \tag{16}$$

where R_0 is the radius of curvature without deformation. Substitution of this area ratio into the Bernoulli's equation gives:

$$\text{2-D}: \quad dp_{gas} = P_1 - P_2 = \frac{\rho u_{in}^2}{2}\zeta_{2D}^2 \tag{17}$$

$$\text{3-D}: \quad dp_{gas} = P_1 - P_3 = \frac{\rho u_{in}^2}{2}\zeta_{3D}^2 \tag{18}$$

Substituting the pressure differences into Eq. (14) yields:

$$\text{2-D}: \quad \frac{dR}{R} = \frac{\rho u_{in}^2 R_0}{4\gamma}\frac{R}{R_0}\zeta_{2D}^2 = \frac{We_r}{4}\frac{R}{R_0}\zeta_{2D}^2 \tag{19}$$

$$\text{3-D}: \quad \frac{dR}{R} = \frac{\rho u_{in}^2 R_0}{4\gamma}\frac{R}{R_0}\zeta_{3D}^2 = \frac{We_r}{4}\frac{R}{R_0}\zeta_{3D}^2 \tag{20}$$

where We_r is the Weber number, defined as the ratio between fluid inertia and surface tension:

$$We_r = \frac{\rho u^2 R_0}{\gamma} \tag{21}$$

2.3. Droplet detachment

2.3.1. Analysis using the control-volume approach

In the occasions that the droplet shape change is negligible, the detachment velocity, defined as the minimum gas velocity to detach the droplet, i.e. $F_{drag} = F_{\gamma x}$, can be estimated based on the force balance over a spherical droplet. Following Chen et al. [13], the force balance along the channel-flow direction of the control volume can be expressed as (see Fig. 3)

$$(p_0' - p_L')2Bl + l^2\tau_{xz}^W + F_{drag} = 0 \tag{22}$$

where $l^2\tau_{xz}^W$ and F_{drag} represent the shear stress on the top wall and drag on the water droplet. By assuming fully developed laminar Newtonian gas flow, the viscous drag can be approximated as [13]

$$-F_{drag} = (p_0' - p_L')(2B - b)l \tag{23}$$

The gas pressure drop across droplet can be related to the overall pressure drop by using average velocity, viscosity and channel height as [13]

$$(p_0' - p_L') = (p_0 - p_L) - (L - l)\frac{3\mu U}{B^2} \tag{24}$$

$$(p_0' - p_L') = \frac{3\mu U'}{b^2}l \tag{25}$$

Based on the mass balance ($U' = (B/b)U$), Eq. (24) can be expressed as [13]

$$(p_0' - p_L') = (p_0 - p_L)\frac{l}{l + (L - l)(b/B)^3} \tag{26}$$

Substitution of Eq. (26) into (23) yields [13]

$$-F_{drag} = (p_0 - p_L)\frac{l^2(2B - b)}{l + (L - l)(b/B)^3} \tag{27}$$

By defining dimensionless droplet height as $\widehat{H} = r(1 - \cos\theta_a)/2B$, Eq. (27) becomes:

$$-F_{drag} = \frac{(p_0 - p_L)B(l/L)^2 L(1 + \widehat{H})}{(1 - \widehat{H})^3 + (l/L)[1 - (1 - \widehat{H})^3]} \tag{28}$$

For a sufficiently large droplet with $\theta_a \geq 90^\circ$, $l = 2r$, the viscous drag can be further simplified in terms of average velocity in the upstream and downstream regions as [13]

$$-F_{drag} = \frac{48\mu UB}{(1 - \cos\theta_a)}\frac{(1 + \widehat{H})\widehat{H}^2}{(1 - \cos\theta_a)(1 - \widehat{H})^3 + (4B/L)\widehat{H}[1 - (1 - \widehat{H})^3]} \tag{29}$$

The adhesion force on the contact line between the wall and droplet can be expressed by considering the advancing and receding contacts:

$$F_{\gamma x} = \pi(r \sin\theta_a)\gamma \cos(180 - \theta_a) + \pi(r \sin\theta_a)\gamma \cos\theta_r \tag{30}$$

When the surface tension force is larger than the viscous drag balance, the droplet will be detached, therefore the critical velocity can be calculated by setting:

$$-F_{drag} = F_{\gamma x} \tag{31}$$

By defining $y = \sin(1/2)(\theta_a - \theta_r)$, substituting Eqs. (29) and (30) into (31) yields:

$$y\sqrt{1 - y^2} - (\cot\theta_s)y^2 - \frac{12\mu U}{\pi\gamma \sin^2\theta_s}\frac{\widehat{H}(1 + \widehat{H})}{(1 - \cos\theta_s)(1 - \widehat{H})^3 + (4B/L)\widehat{H}[1 - (1 - \widehat{H})^3]} = 0 \tag{32}$$

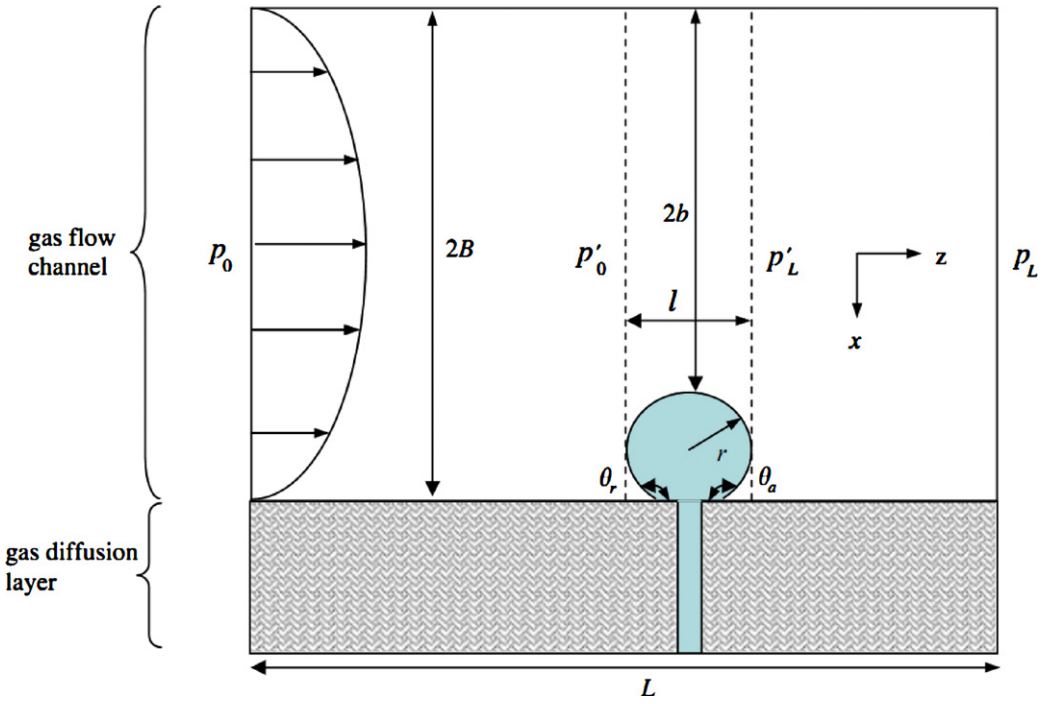

Fig. 3. Control volume enclosing the liquid water droplet [13].

This above expression can be further rearranged:

$$y\sqrt{1-y^2} - (\cot\theta_s)y^2 - Re^{-1}\mathrm{We}_r\frac{H}{r}\frac{12}{\pi\sin^2\theta_s}\frac{\widehat{H}(1+\widehat{H})}{(1-\cos\theta_s)(1-\widehat{H})^3 + (4B/L)\widehat{H}[1-(1-\widehat{H})^3]} = 0 \quad (33)$$

2.3.2. Derivation using the drag coefficient (C_D)

Another method that can be used to estimate the droplet detachment velocity the drag coefficient C_D defined by:

$$C_D = \frac{F_{drag}/A_p}{(1/2)\rho U^2} \quad (34)$$

where A_p is the projected area of the droplet which is estimated as $A_p = (\theta_s - \sin\theta_s\cos\theta_s)d^2/4$. The drag coefficient is determined by the Reynolds number. Chen [14] adopted the following formula:

$$C_D = \frac{30}{\sqrt{Re_H}}, \quad Re_H = \frac{\rho UH}{\mu} \quad (35)$$

The surface tension force (Eq. (30)) can be simplified as:

$$F_{\gamma x} = \pi d\gamma\sin^2\theta_s\sin\frac{1}{2}(\theta_a - \theta_r) \quad (36)$$

Again, the critical gas velocity can be obtained by setting $F_{drag} = F_{\gamma x}$ [14]:

$$U_c = \left[\frac{H}{\rho\mu}\right]^{1/3}\left[\frac{4}{15}\frac{\pi\gamma\sin^2\theta_s\sin(1/2)(\theta_a-\theta_r)}{(\theta_s - \sin\theta_s\cos\theta_s)d}\right]^{2/3} \quad (37)$$

A simplified relation between the Weber number and Reynolds number can be obtained from the above equation:

$$\mathrm{We}_r Re_H^{-0.5} = \frac{2}{15}\frac{\pi\sin^2\theta_s\sin(1/2)(\theta_a-\theta_r)}{(\theta_s - \sin\theta_s\cos\theta_s)} \quad (38)$$

3. Numerical simulation

In order to evaluate the forces on a liquid droplet in a gas flow channel, the 3-D Navier–Stokes equations for incompressible viscous flow are solved numerically:

$$\nabla\cdot(\rho\vec{v}) = 0 \quad (39)$$

$$\nabla\cdot(\rho\vec{v}\vec{v}) = -\nabla p + \nabla\cdot\mu\left[(\nabla\vec{v} + \nabla\vec{v}^T) - \frac{2}{3}\nabla\cdot\vec{v}I\right] + \rho\vec{g} \quad (40)$$

In this evaluation, we assume negligible deformation, thus the droplet has a spherical-cap shape. We also assume the non-slip condition of the gas flow on the droplet surface. Fig. 4 shows the computational domain with boundaries. The computational domains are built with about 1.3 million hexahedral cells (which was arrived at after a grid-independent study). Air flow is introduced through uniform velocity at inlet boundary uniformly and it exits through pressure outlet boundary. Due to symmetry, only half of the channel is simulated. Non-slip condition is applied to all wall boundaries. Various droplet sizes are considered and air flow velocity is set between 0.5 and 10.0 m s^{-1} based on previous studies (e.g. [13,14]). Details of the cases considered for numerical simulation are presented in Table 1. A commercial CFD code (Fluent 6.3.26) was used to solve the highly nonlinear governing equations.

4. Results and discussion

4.1. Force components

In real-world PEFC operations, the maximum possible air velocity in a channel with a static droplet on the GDL surface is limited by the detachment velocity. For a parametric study on the forces over a droplet, the gas velocity is allowed to exceed that limit while the droplet remains static. Fig. 5 shows the two drag forces (Eqs. (2)–(4)) as a function of the gas velocity. Various droplet sizes are compared and results are presented for fully developed region (Case 1) and the entrance region (Case 2). As expected, both pressure and viscous force increase rapidly with the gas velocity. For

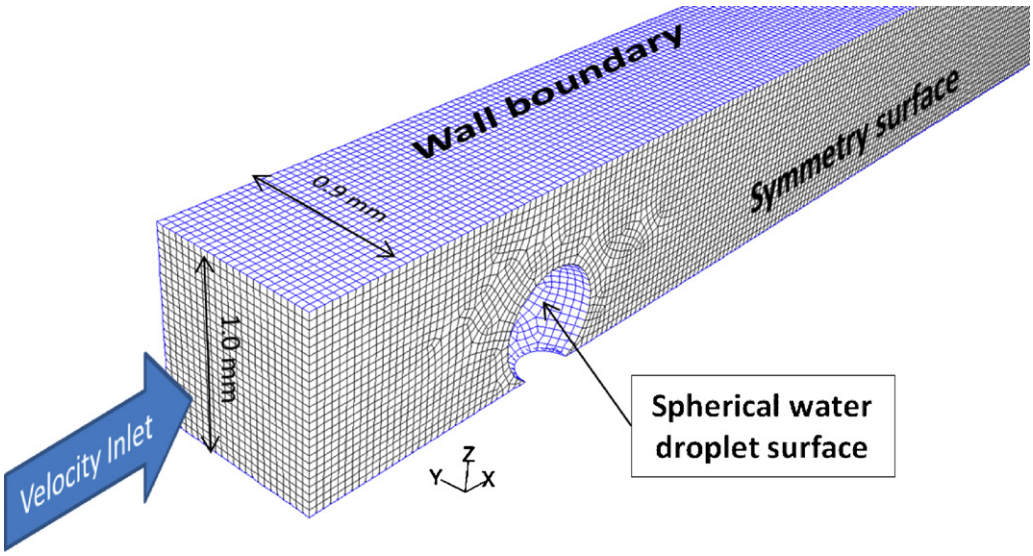

Fig. 4. The 3-D computational domain and boundary condition for Case 2.

Table 1
List of numerical simulation cases.

Case no.	Working fluid	Flow condition	Channel dimension (mm^3)	Contact angle	Contact angle hysteresis	Droplet diameter (mm)	Air flow velocity ($m\,s^{-1}$)
1	Air	Fully developed					
2	Air	Entrance length	$1.8 \times 1.0 \times 23$	150°	10°	0.1–0.6	0.5–10.0
3	Hydrogen	Fully developed					

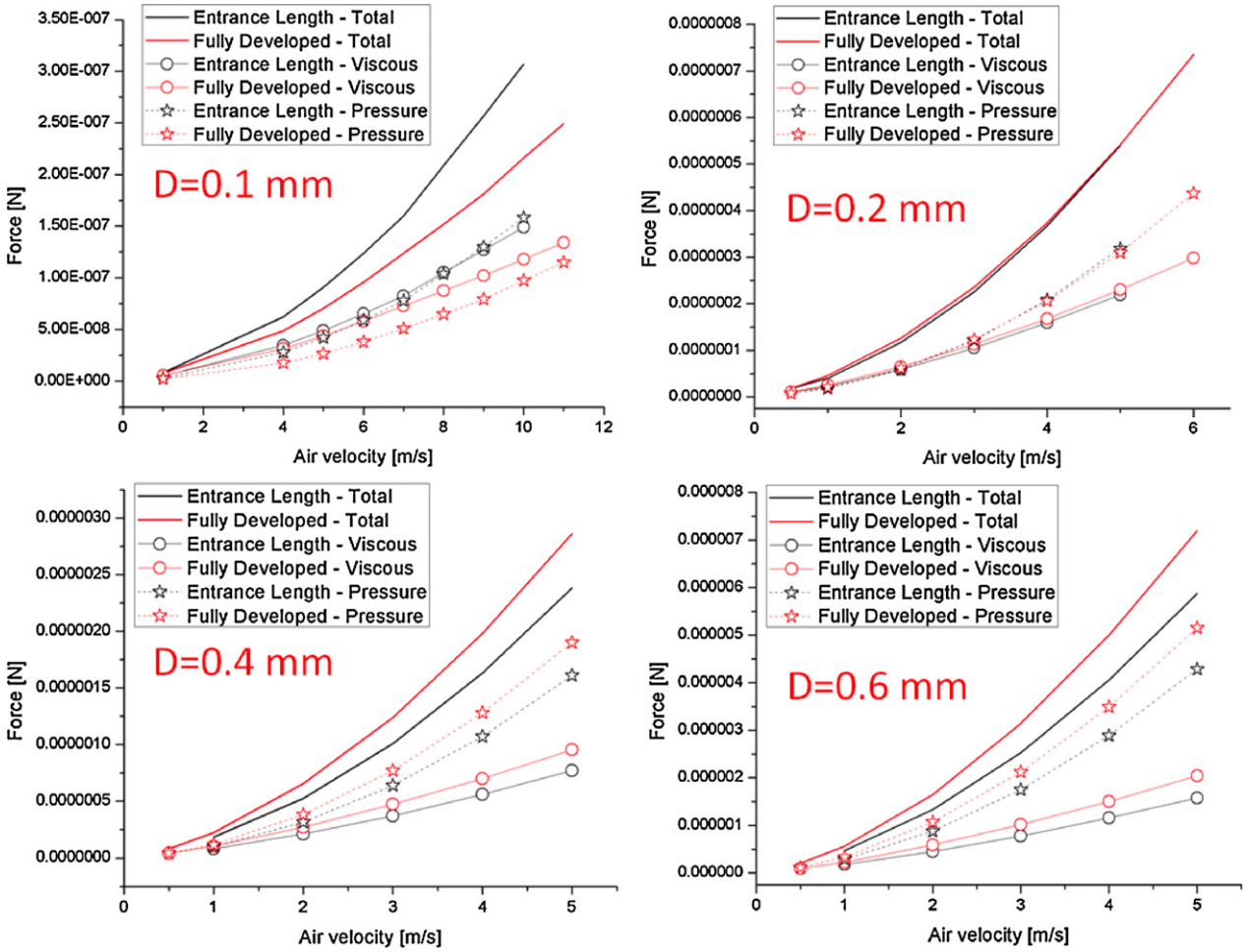

Fig. 5. Comparison of drag forces between the entrance and fully developed regions (Case 1 and Case 2).

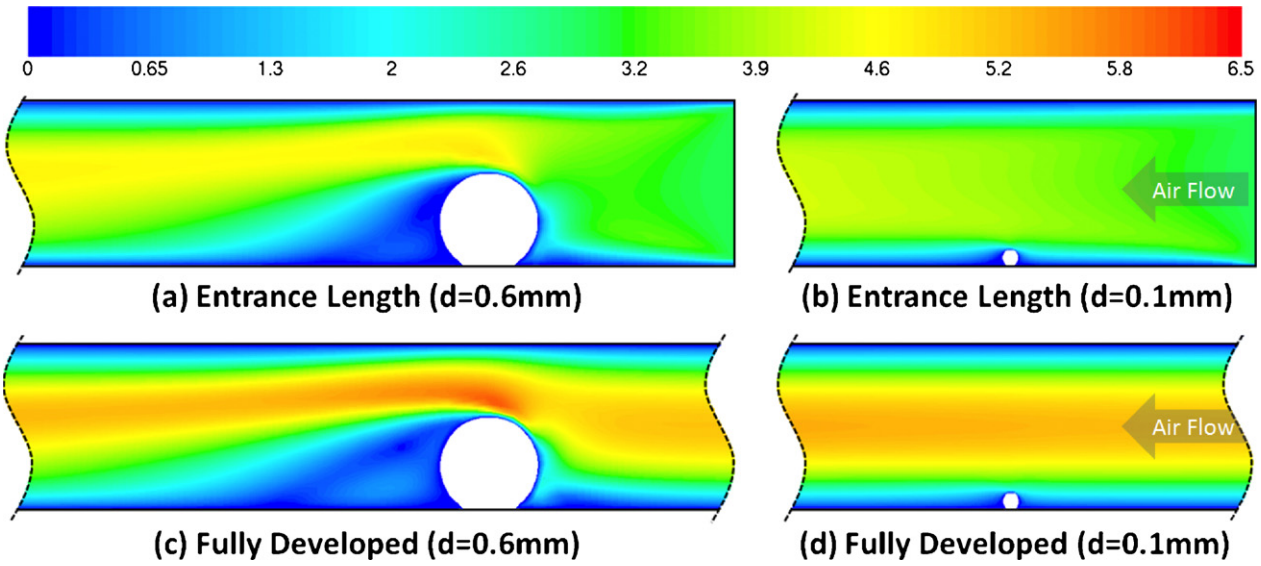

Fig. 6. Velocity contours in the entrance (a and b) and fully developed (c and d) regions, respectively ($u_{in} = 3.0\,m\,s^{-1}$).

small droplets, the viscous force dominates, while the pressure drag becomes more important for relatively large droplets. Fig. 5 also compares the forces for two typical locations in a channel, i.e. the entrance (Case 2) and fully developed regions (Case 1), which show flow in distinct regimes. Many studies only considered a fully developed channel flow in fuel cells because of the large ratio of the channel length to cross-section dimension. In the entrance length, the boundary layer is undergoing development, and due to the

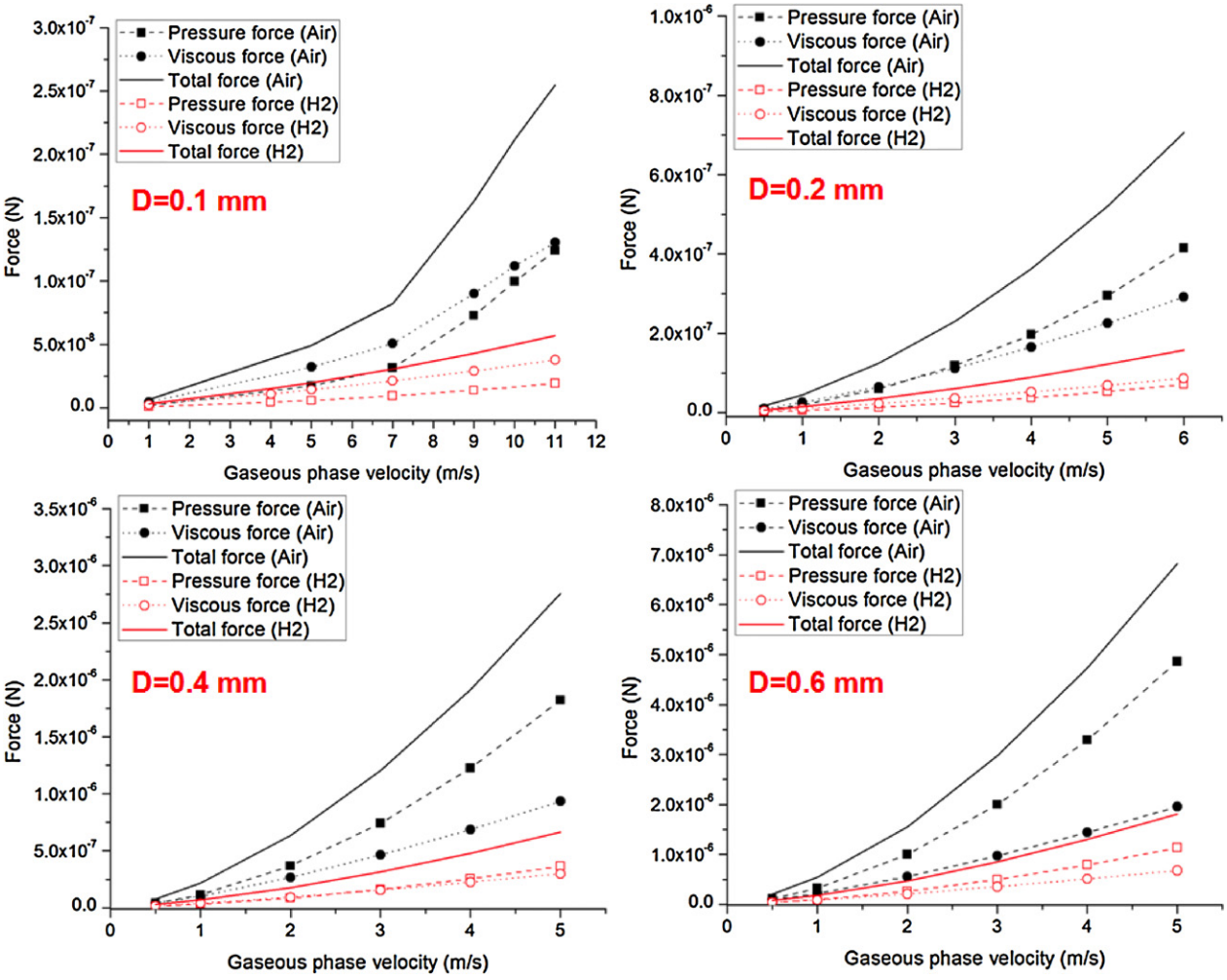

Fig. 7. Drag forces for air and hydrogen flows, respectively, at various droplet diameters (Case 1 and Case 3).

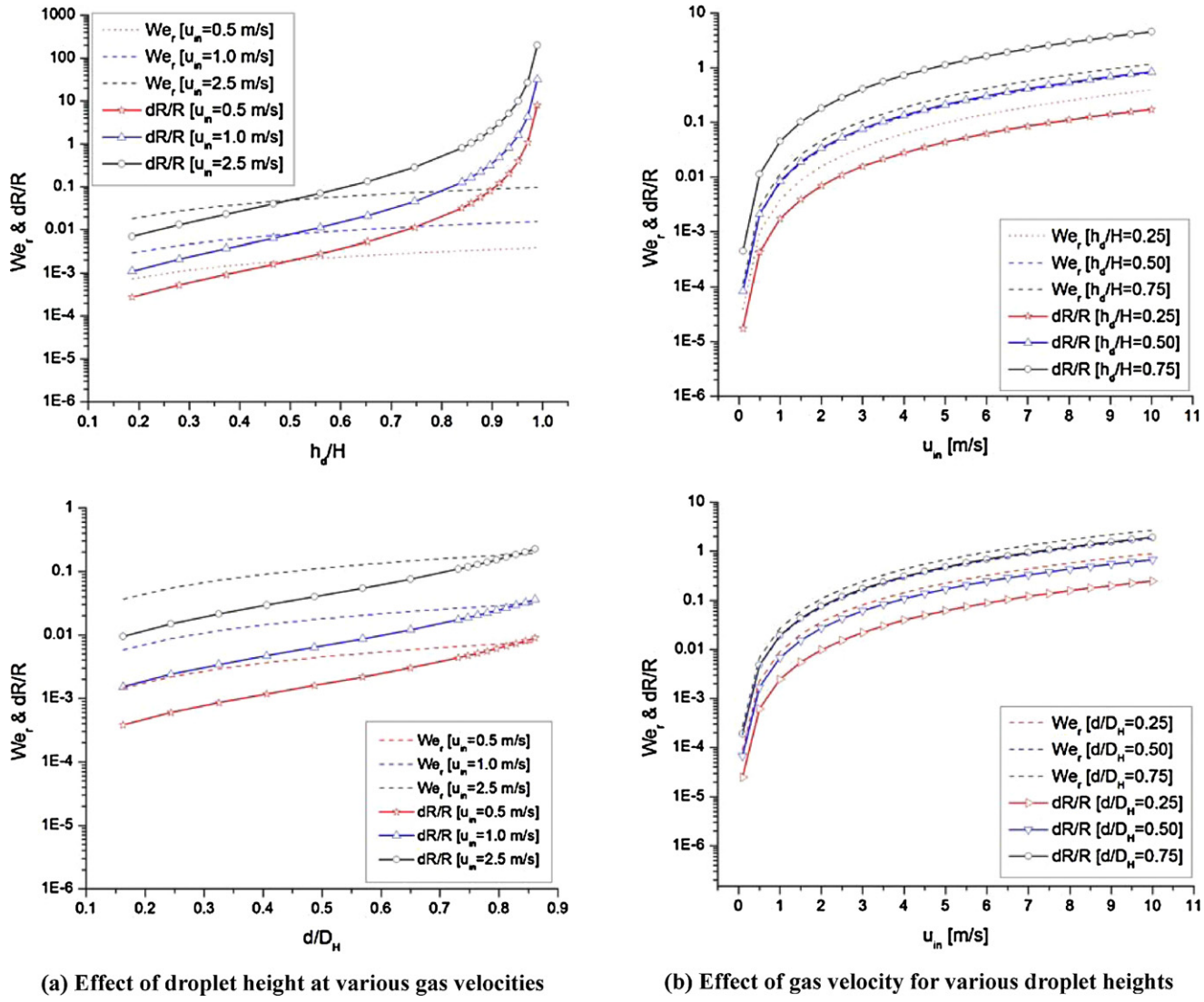

Fig. 8. Droplet deformation in air flow (2-D and 3-D) calculated by Eqs. (19) and (20). (a) Effect of droplet height at various gas velocities; (b) effect of gas velocity for various droplet heights.

momentum diffusion, the boundary layer will grow and eventually meet at the centerline. After that, the channel flow reaches the fully developed stage with a parabolic velocity profile. In PEFCs, the Reynolds number of channel flows is usually relatively small or moderate (that is, not exceedingly large) such that flow is in the laminar regime. The hydrodynamic entrance length L_E can be evaluated using that developed in tube laminar flow: $L_E/d \sim 0.06\mathrm{Re}$, where d is the tube diameter. A Re of 200 will lead to $L_E \sim 12d$, which is small but not negligible. For a 1.0 mm diameter tube, the entrance length is around 12 mm, which is about 10% of a 10 cm length channel. The velocity profiles near the water droplet for both near entrance and fully developed conditions are plotted in Fig. 6. In the entrance region, a small droplet ($d < 0.2$ mm) experiences a stronger force than that in the fully developed region. This can be explained by that in the entrance region the gas velocity is almost uniform in the gas channel, therefore the velocity around small droplets on the wall undergoes larger surrounding gas flows in comparison with the fully developed region. As a result, the detachment velocity of a small droplet is lower in the entrance region than that in the fully developed condition. As the droplet size increases, the pressure force becomes dominant. In the fully developed region, the local air velocity in the core of the channel is higher than the average value that approximately equals to the nearly uniform velocity in the entrance region. A large droplet will physically extend to the core region, facing a higher air velocity in the fully developed region. Since the pressure force is approximately proportional to the square of the gas velocity magnitude, a larger droplet experiences a larger drag force, i.e. a lower detachment velocity is in the fully-developed region than in the entrance region. When the working fluid is switched to hydrogen (i.e. in the anode gas flow channel), the magnitude of the forces decreases by about an order, as shown in Fig. 7, due to the lower gas density. Note that many studies indicated that liquid can emerge on the anode side [12,28,29]. If droplets eventually form on the anode GDL surface, it can be difficult to remove them.

4.2. Droplet shape change

To examine droplet shape changes under various conditions, the ratio of local curvature change to the initial surface curvature (Eqs. (19) and (20)) is plotted in Fig. 8. The droplet height is normalized by the channel height for 2-D and droplet diameter is normalized by the hydraulic diameter of the gas channel for 3-D. The droplet deformation rapidly increases with the droplet height, particularly

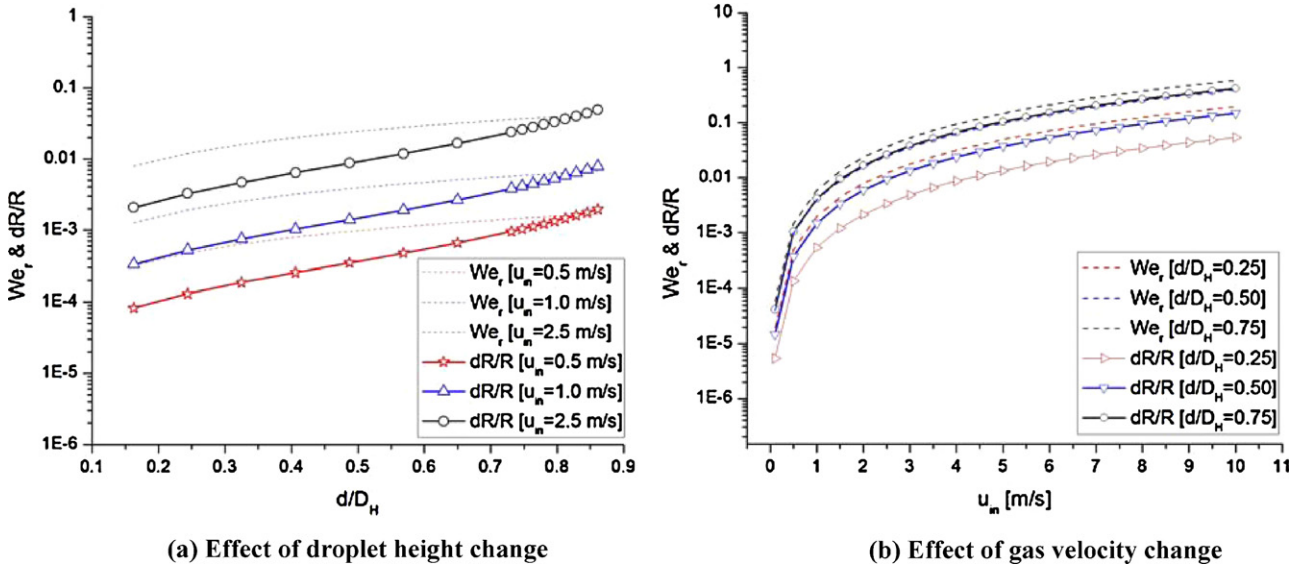

Fig. 9. Droplet deformation in hydrogen channel flow (3-D) calculated by Eq. (20). (a) Effect of droplet height change; (b) effect of gas velocity change.

when approaching the channel height. The reason is that the acceleration of gas flow around the droplet due to its obstruction lowers the local gas pressure. The increasing rate is much faster for the 2-D case than the 3-D case because the domain of the latter has four corners which can allow gas flow to pass through. In addition, the deformation magnitude increases with the air velocity, as expected. At low air velocity, the forces by the gas flow are weak, leading to a small Weber number and hence small deformation. It can be seen that the deformation is usually smaller than 10% when the gas flow velocity is less than 1.0 m s^{-1} for both 2-D and 3-D cases. Even for the cases with velocity smaller than 5 m s^{-1}, the droplet deformation is smaller than 10% for the 3-D cases. Therefore, to a good approximation we can neglect the effect of droplet shape change in gas flow channels for most operating condition, which simplifies the analysis. Fig. 9 shows the parametric study of droplet deformation in hydrogen gas flow. The magnitude of droplet deformation is smaller than that for the flowing air, which is due to the smaller density of hydrogen flow.

4.3. Detachment velocity

The drag coefficient C_D is a dimensionless parameter characterizing the drag force on an object in fluid flow. Many correlations of the drag coefficient as a function of the Reynolds number (Re) have been developed for objects in unconfined flows. Similar approach can be taken for the drag coefficient over a droplet inside channels. In the range of Re for typical fuel cell operation, the drag coefficient of various droplet diameters are numerically calculated using the 3-D simulation results, which are plotted in Fig. 10. It can be seen that the one used by Chen [14] (Eq. (38)) gives a fair agreement, but exhibits deviation for small droplets ($d \sim 0.1$ mm). It might be impossible to use one formula to describe the full ranges of gas flow and channel dimension. A generalized approach can be expressed:

$$C_D = a \times Re_H^b \tag{41}$$

In this study, the fitting parameters for the fully developed condition are:

$$a = 46.247 \times \left(\frac{D}{H}\right)^{0.1757}, \quad b = 0.2158 \times \left(\frac{D}{H}\right) - 0.6384$$

By using this expression, Eq. (38) can be changed to:

$$We_r Re_H^b = \frac{4}{a} \frac{\pi \ \sin^2 \theta_s \ \sin(1/2)(\theta_a - \theta_r)}{(\theta_s - \sin \theta_s \ \cos \theta_s)} \tag{42}$$

Fig. 11 plots the detachment velocity for various droplet sizes for both air and hydrogen flows using Eq. (42). It is observed that the detachment velocity dramatically increases as droplet diameter decreases. This trend is well matched to the previous findings reported in the literature [16,17]. The detachment velocity is also sensitive to the contact angle and contact-angle hysteresis: as the contact angle decreases and the contact-angle hysteresis increases, the detachment velocity becomes larger. Since the hydrogen flow exerts a smaller drag force on a droplet, higher gas velocities are required to detach water droplet in the anode side. Fig. 12 displays the comparison of the Re–We relations at the detachment velocity at various droplet sizes among the models, i.e. Eqs. (33), (38) and (42). Contact angle and contact-angle hysteresis are set at 150° and 10°, respectively, and channel length is assumed as 4.5 cm

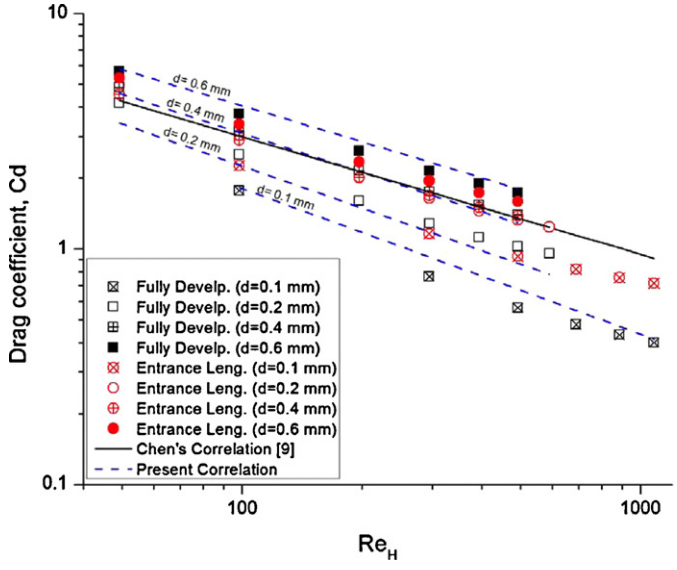

Fig. 10. Drag coefficients in a micro channel at various conditions.

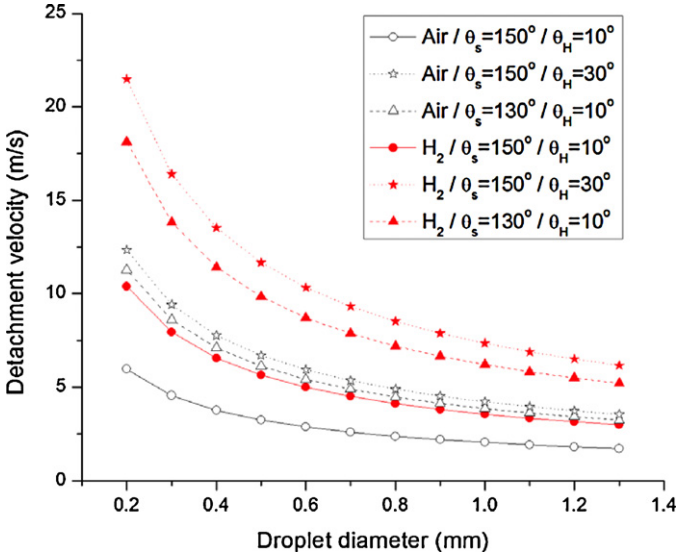

Fig. 11. Detachment velocities in air flow and hydrogen (H_2) flows, respectively, calculated by Eq. (42).

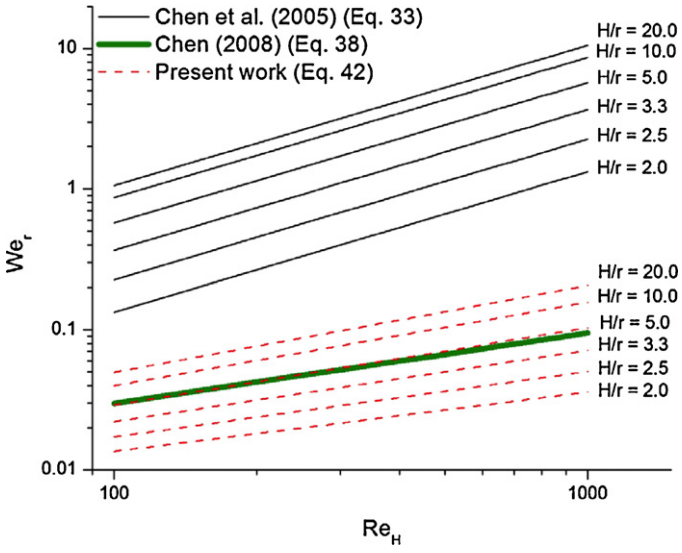

Fig. 12. The We–Re relation at various droplet sizes calculated by Eqs. (33), (38) and (42), respectively.

for comparison. It can be seen that the Weber number increases with the Reynolds number at the detachment velocities. As droplet size increases, the Weber number decreases since less drag force is required for detachment. The correlation used by Chen [14] shows a higher Weber number, which gives the upper bound of the droplet stable region.

While several important analytical solutions of droplet dynamics such as deformation and detachment are obtained in the present work, it is important to compare model prediction with experimental data. In the follow-on work as presented in our sequel paper, we will present extensive experimental work on droplet deformation and detachment and comparison between experimental and simulation (or model prediction) results. In addition, the VOF simulation provides detail of two-phase flow along with the interface track. We will report results from both 2-D and 3-D VOF studies and compare their predictions with the analytical solutions presented in this paper.

5. Conclusion

In this study, water droplet dynamics in a PEFC gas flow channel was analyzed. The drag forces on a droplet were computed and compared under various conditions. We found that the viscous force has significant impact on a small droplet in low gas velocity regime whereas the pressure drag is important for a large droplet when the gas flows relatively slowly. Small droplets in the entrance region get more drag than that under fully developed condition while a large droplet experiences greater drag under the fully developed condition. When hydrogen is used as the flowing gas, both pressure and viscous drags are reduced. Droplet deformation was also analyzed and a formula was derived to quantify the deformation caused by pressure variation at two typical locations. We found that droplet deformation is fairly small in most cases, but significant shape change may occur at high gas velocities and large droplet sizes. Further, the drag coefficient over a droplet in a gas flow channel was computed and a model was developed to predict the detachment velocity. We found that the Weber number increases with Reynolds number at the detachment velocity and decreases with growing droplet size. In the follow-on work that will be reported in a sequel paper, we will present experimental results and extensive VOF simulation to validate the analytical solutions of the droplet deformation and removal reported in the present work.

References

[1] Y. Wang, K.S. Chen, J. Mishler, S.C. Cho, X.C. Adroher, Appl. Energy 88 (2011) 981–1007.
[2] C.Y. Wang, Chem. Rev. 104 (2004) 4727–4766 (Washington, DC).
[3] A.Z. Weber, J. Newman, Chem. Rev. 104 (2004) 4679–4726 (Washington, DC).
[4] K. Jiao, X. Li, Prog. Energy Combust. Sci. 37 (3) (2011) 221–291.
[5] N. Khajeh-Hosseini-Dalasm, K. Fushinobu, K. Okazaki, J. Electrochem. Soc. 157 (10) (2010) B1358–B1369.
[6] A.D. Le, B. Zhou, Electrochim. Acta 54 (8) (2009) 2137–2154.
[7] H. Meng, J. Power Sources 171 (2) (2007) 738–746.
[8] Y. Wang, J. Electrochem. Soc. 156 (10) (2009) B1134–B1141.
[9] Y. Wang, S. Basu, C.Y. Wang, J. Power Sources 179 (2008) 603–617.
[10] Z. Lu, M.M. Daino, C. Rath, S.G. Kandlikar, Int. J. Hydrogen Energy 35 (2010) 4222–4233.
[11] Y. Ding, H.T. Bi, D.P. Wilkinson, J. Power Sources 195 (2010) 7278–7288.
[12] S. Ge, C.Y. Wang, J. Electrochem. Soc. 154 (10) (2007) B998–B1005.
[13] K.S. Chen, M.A. Hickner, D.R. Noble, Int. J. Energy Res. 29 (2005) 1113–1132.
[14] K.S. Chen, Sixth International Conference on Fuel Cell Science Engineering and Technology, Denver, Colorado, FUELCELL2008-65137, 2008.
[15] E.C. Kumbur, K.V. Sharp, M.M. Mench, J. Power Sources 161 (2006) 333–345.
[16] A. Theodorakakos, T. Ous, M. Gavaises, J.M. Nouri, N. Nikolopoulos, H. Yanagihara, J. Colloid Interface Sci. 300 (2006) 673–687.
[17] X.C. Adroher, Y. Wang, J. Power Sources 196 (2011) 9544–9551.
[18] G. He, P. Ming, Z. Zhao, A. Abdula, Y. Xiao, J. Power Sources 163 (2007) 864–873.
[19] C.H. Schillberg, S.G. Kandlikar, Proceeding of the Fifth International Conference on Nanochannels Microchannels and Minichannels, ICNMM2007-30029, 2007.
[20] J.H. Nam, M. Kaviany, Int. J. Heat Mass Trans. 46 (2003) 4595–4611.
[21] T. Ous, C. Arcoumamis, J. Power Sources 173 (2007) 137–148.
[22] E. Shirani, S. Masoomi, J. Fuel Cell Sci. Technol. 5 (2008) 041008.
[23] X. Zhu, P.C. Sui, N. Djilali, J. Power Sources 172 (2007) 287–295.
[24] X. Zhu, Q. Liao, P.C. Sui, N. Djilali, J. Power Sources 195 (2010) 801–812.
[25] C. Fang, C. Hidrovo, F. Wang, J. Eaton, K. Goodson, Int. J. Multiphase Flow 34 (2008) 690–705.
[26] G. Falcone, G.F. Hewitt, C. Alimonti, Multiphase Flow Metering: Principles and Applications, 1st ed., Elsevier, 2009.
[27] A.W. Adamson, A.P. Gast, Physical Chemistry of Surfaces, 6th ed., John Wiley & Sons, Inc., 1997.
[28] Y. Wang, K.S. Chen, J. Electrochem. Soc. 157 (12) (2010) B1878–B1886.
[29] Y. Wang, J. Power Sources 185 (2008) C261–C271.
[30] S. Tasoglu, G. Kaynak, A.J. Szeri, U. Demirci, M. Muradoglu, Phys. Fluids 2 (2010) 082103.